J. Fluid Mech. (1998), *vol.* 377, *pp.* 27–45. Printed in the United Kingdom

Spouting and planform selection in the Rayleigh–Taylor instability of miscible viscous fluids

By N. M. RIBE†

Institut de Physique du Globe, 4 place Jussieu, 75252 Paris cédex 05, France

(Received 24 September 1997 and in revised form 13 July 1998)

A weakly nonlinear analysis is used to study the initial evolution of the Rayleigh–Taylor instability of two superposed miscible layers of viscous fluid between impermeable and traction-free planes in a field of gravity. Analytical solutions are obtained to second order in the small amplitude of the initial perturbation of the interface, which consists of either rolls or squares or hexagons with a horizontal wavenumber k. The solutions are valid for arbitrary values of k, the viscosity ratio (upper/lower) γ, and the depth ratio r, but are presented assuming that $k = k_{max}(\gamma, r)$, where k_{max} is the most unstable wavenumber predicted by the linear theory. For all planforms, the direction of spouting (superexponential growth of interfacial extrema) is determined by the balance between the tendency of the spouts to penetrate the less viscous layer, and a much stronger tendency to penetrate the thicker layer. When these tendencies are opposed (i.e. when $\gamma > 1$ with $r > 1$), the spouts change direction at a critical value of $r = r_c(\gamma)$. Hexagons with spouts at their centres are the preferred planform for nearly all values of γ and r, followed closely by squares; the most slowly growing planform is hexagons with spouts at corners. Planform selectivity is strongest when $\gamma \geqslant 10$ and $r \geqslant \gamma^{1/3}$. Application of the results to salt domes in Germany and Iran show that these correspond to points (γ, r) below the critical curve $r = r_c(\gamma)$, indicating that the domes developed from interfacial extrema having subexponential growth rates.

1. Introduction

When a dense fluid lies above a lighter in a field of gravity, the interface between them is inherently unstable to small perturbations. This is the classic form of the so-called Rayleigh–Taylor (henceforth RT) instability, first studied theoretically by Rayleigh (1883). Later, Taylor (1950) showed that acceleration of the fluid interface produces the same effect as gravity, whence the compound name by which this instability is now known. Chandresekhar (1961) reviewed the linear theory of RT instability for two infinite fluids with equal kinematic viscosities separated by an interface with surface tension. The instability has subsequently been investigated in a wide variety of systems and contexts: inviscid and viscous fluids, miscible and immiscible fluids, infinite and bounded domains, infinitesimal and finite amplitude, and two- and three-dimensional flow.

This study focuses on the case of highly viscous fluids in which the effects of inertia

---

† Permanent address: Department of Geology and Geophysics, Yale University, PO Box 208109, New Haven, CT 06520-8109, USA.

can be neglected. The principal motivation is geophysical: the RT instability has been invoked as a simple model for such diverse phenomena as salt domes (Nettleton 1934), mantled gneiss domes (Fletcher 1972), island-arc volcanism (Marsh & Carmichael 1974), the formation of mantle plumes (Whitehead & Luther 1975), mid-ocean ridge volcanism (Whitehead 1986), subduction of oceanic lithosphere (Canright & Morris 1993), and instability of continental lithosphere beneath mountain belts (Houseman & Molnar 1997).

The RT instability of very viscous fluids has been studied extensively using analytical, numerical, and experimental methods. Most of the extant analytical studies are limited to linear stability analysis. The earliest such studies considered simple two-layer models (Daneš 1964; Selig 1965), and were later extended to multiple layers and different boundary conditions; for reviews and bibliographies, see Ramberg (1981) and Johnson & Fletcher (1994). By contrast, there have been few analytical studies in the nonlinear regime. Whitehead & Luther (1975), following a suggestion of Daneš (1964), examined the effect of nonlinear convection of the interface during the initial stages of the instability. They concluded that a hexagonal planform should be preferred, and attempted to determine the direction of 'spouting' (superexponential growth of interfacial extrema) in a two-layer system. However, their theory neglected the nonlinearities associated with the matching conditions at the interface. Another approach has been to simplify the governing equations by assuming that the dominant wavelength greatly exceeds the layer thickness, due either to surface tension (Babchin *et al.* 1983; Yiantsios & Higgins 1989; Fermigier *et al.* 1992) or to an extreme viscosity contrast (Canright & Morris 1993).

Numerical techniques such as finite elements (Woidt 1978; Schmeling 1987; Houseman & Molnar 1997) and the boundary integral method (Newhouse & Pozrikides 1990) have also been used to study the large-amplitude evolution of the viscous RT instability. However, all numerical approaches to date have been limited to two-dimensional and axisymmetric geometries, and with rare exceptions (Schmeling 1987; Houseman & Molnar 1997) have emphasized the qualitative morphology of the instability rather than quantitative scaling laws.

Experimental work on the viscous RT instability includes the study of Whitehead & Luther (1975), who performed experiments under normal gravity and showed that the morphology of the spouts depends on the viscosity contrast. An alternative approach has been to use extremely viscous fluids (e.g. silicone putties) and to enhance the effective gravity by spinning in a centrifuge (e.g., Ramberg 1981; Jackson & Talbot 1989). In general, laboratory experiments have proven to be powerful tools for studying the morphology of the RT instability, but have yielded few quantitative results.

In summary, despite extensive previous study, quantitative understanding of the viscous RT instability remains limited. This study investigates two questions that remain unresolved: in what direction (up or down) does spouting occur in a system of two layers with arbitrary thicknesses and viscosities? And in the same system, what horizontal planform is preferred? Answers to these questions are provided by an analytical weakly nonlinear solution for the early evolution of the instability that is valid for arbitrary values of the wavelength, the viscosity ratio, and the layer thickness ratio. The results are then applied to salt dome fields in Germany and Iran. Readers who wish to skip the mathematical details will find a self-contained summary of the model and conclusions in § 7.

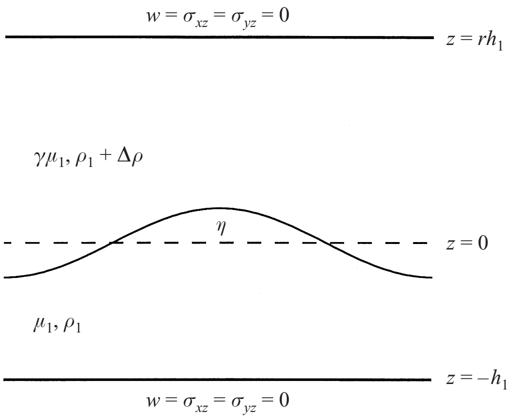

FIGURE 1. Definition sketch of the model. Two layers of highly viscous fluid are confined between impermeable and traction-free planes. The lower layer has thickness h_1, viscosity μ_1, and density ρ_1, and the upper layer has thickness $h_2 \equiv rh_1$ $(r > 1)$, viscosity $\mu_2 \equiv \gamma\mu_1$, and density $\rho_1 + \Delta\rho$. The deformation of the interface (initially at $z = 0$) is $\eta(x, y, t)$, and surface tension between the fluids is neglected.

2. Model definition and equations

The model to be studied is sketched in figure 1. A layer $-h_1 \leqslant z \leqslant 0$ of fluid with viscosity μ_1 and density ρ_1 lies beneath another layer $0 \leqslant z \leqslant rh_1$ with viscosity $\mu_2 \equiv \gamma\mu_1$ and density $\rho_2 = \rho_1 + \Delta\rho$. Both bounding surfaces are traction-free and impermeable. Because both boundary conditions are the same, one can assume $r \geqslant 1$ with no loss of generality. At time $t = 0$, the interface between the layers is perturbed by an amount $\epsilon h_1 f(x, y)$, and its position thereafter is $z = h_1\eta(x, y, t)$. The fluids are assumed to be perfectly miscible (no surface tension), and to have negligible inertia (creeping flow). Both of these assumptions are valid for flow within the Earth's mantle and crust.

Throughout this study, lengths are non-dimensionalized by h_1, velocities by $\Delta\rho g h_1^2/\mu_1$, time by $\mu_1/\Delta\rho g h_1$, and stresses by $\Delta\rho g h_1$. All variables appearing in the equations below are dimensionless.

The velocity within each fluid can be represented as

$$\boldsymbol{u} = \nabla \times \nabla \times \Phi\boldsymbol{z} + \nabla \times \Psi\boldsymbol{z} \equiv \left(\Phi_{xz} + \Psi_y\right)\boldsymbol{x} + \left(\Phi_{yz} - \Psi_x\right)\boldsymbol{y} - \nabla_h^2\Phi\boldsymbol{z}, \tag{2.1}$$

where Φ is the poloidal potential, Ψ is the toroidal potential, $\boldsymbol{x}$, $\boldsymbol{y}$, and $\boldsymbol{z}$ are unit vectors, ∇_h^2 is the horizontal Laplacian, and subscripts denote partial differentiation. The potentials satisfy the equations

$$\nabla^4\Phi = \nabla^2\Psi = 0 \tag{2.2}$$

subject to the boundary conditions $\Phi = \mathrm{D}^2\Phi = \mathrm{D}\Psi = 0$ at $z = -1$ and $z = r$, where $\mathrm{D} = \partial/\partial z$ (or $\mathrm{d}/\mathrm{d}z$ in what follows, depending on the context). Matching of velocity and stress at the interface requires

$$\langle\boldsymbol{u}\cdot\boldsymbol{n}\rangle = \langle\boldsymbol{u}\cdot\boldsymbol{t}\rangle = \langle\boldsymbol{t}\cdot\boldsymbol{\sigma}\cdot\boldsymbol{n}\rangle = \langle\boldsymbol{n}\cdot\boldsymbol{\sigma}\cdot\boldsymbol{n}\rangle + \eta = 0, \tag{2.3}$$

where $\langle\,\rangle$ denotes the jump in the enclosed quantity from fluid 1 to fluid 2 across the interface $z = \eta$, $\boldsymbol{\sigma}$ is the non-hydrostatic stress tensor,

$$\boldsymbol{n} = \left(1 + |\nabla_h\eta|^2\right)^{-1/2}(-\nabla_h\eta + \boldsymbol{z}) \tag{2.4}$$

is a unit vector normal to the interface,

$$\boldsymbol{t} = \left[1 + (\boldsymbol{c}\cdot\nabla_h\eta)^2\right]^{-1/2}\left[\boldsymbol{c} + (\boldsymbol{c}\cdot\nabla_h\eta)\boldsymbol{z}\right] \tag{2.5}$$

is a unit vector parallel to the interface, $\boldsymbol{c} = \cos\theta\boldsymbol{x} + \sin\theta\boldsymbol{y}$, and θ is the azimuth of the horizontal part of $\boldsymbol{t}$. Finally, the nature of the interface as a material surface requires

$$\frac{\partial\eta}{\partial t} + \boldsymbol{u}\cdot\nabla_h\eta = w(\eta), \tag{2.6}$$

where $w(\eta)$ is the vertical velocity of the interface $z = \eta$. Following the example of (2.6), I shall henceforth suppress the arguments x, y, and t for clarity.

3. Weakly nonlinear analysis

If the initial amplitude ϵ of the perturbed interface is small, the solutions for Φ, Ψ, and η have the forms

$$\Phi = \epsilon\Phi_1 + \epsilon^2\Phi_2 + O(\epsilon^3), \tag{3.1a}$$

$$\Psi = \epsilon^2\Psi_2 + O(\epsilon^3), \tag{3.1b}$$

$$\eta = \epsilon\eta_1 + \epsilon^2\eta_2 + O(\epsilon^3). \tag{3.1c}$$

The matching conditions must be applied at a convected interface whose position is not known in advance. Following a now-classic procedure, these conditions are referred to the reference level $z = 0$ by expanding them in Taylor series. The power series expansions for Φ, Ψ, η, $\boldsymbol{n}$ and $\boldsymbol{t}$ are then substituted into the governing equations and matching conditions, and all terms proportional to each power of ϵ are gathered together. The original nonlinear problem is thereby reduced to a set of linear (but inhomogeneous) problems that can be solved in sequence. A similar analysis has been applied to the inviscid RT instability by Jacobs & Catton (1988).

3.1. $O(\epsilon)$ problem

The $O(\epsilon)$ problem corresponds to a linear stability analysis (e.g. Canright & Morris 1993). The flow at this order is purely poloidal, and the solution has the form

$$\Phi_1 = \phi(z,k)f(x,y)\exp\alpha(k)t, \qquad \eta_1 = f(x,y)\exp\alpha(k)t, \tag{3.2a,b}$$

where f is a planform function satisfying $\nabla_h^2 f = -k^2 f$ and $\alpha(k)$ is the growth rate of an infinitesimal perturbation with wavenumber k. Explicit expressions for $\phi(z,k)$ and $\alpha(k)$ are given in Appendix A.

Figure 2 shows $\alpha(k)$ for (a) $r = \infty$ (an infinitely deep upper layer) and (b) $r = 1$ (layers of equal depth), for several values of the viscosity contrast γ. When $r = \infty$, the growth rate curves exhibit two limiting forms for small and large values of γ. The first, the 'hard-film' limit $r^{-5} \ll \gamma \ll k \ll 1$, corresponds to long-wavelength instability of a high-viscosity layer beneath an effectively infinite fluid with a much lower viscosity. The growth rate curve has a broad and flat top, and the asymptotic expressions for α and the most unstable wavenumber k_{max} are

$$\alpha = \frac{1}{4}\left[1 - \frac{\gamma}{2k} - \frac{k^4}{45}\right], \qquad k_{max} = \tfrac{1}{2}(180\gamma)^{1/5}. \tag{3.3a,b}$$

At the other extreme is the 'soft-film' limit $r^{-1} \ll k \ll 1$, $\gamma \gg k^{-1}$, corresponding to a low-viscosity layer beneath an effectively infinite fluid with a much higher viscosity.

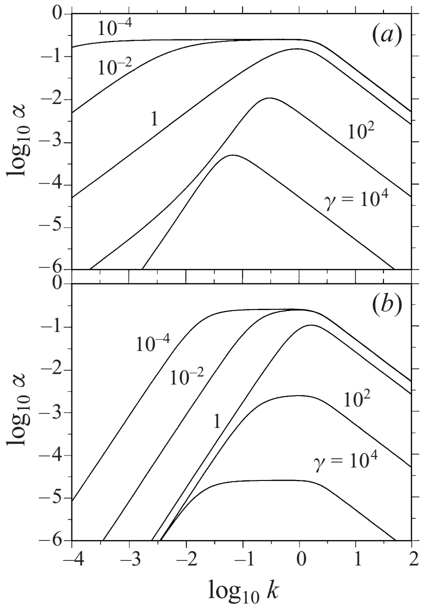

FIGURE 2. Growth rate α as a function of wavenumber k, for several values of the viscosity contrast γ and for layer depth ratios (a) $r = \infty$ and (b) $r = 1$. When $r = 1$, curves for γ and $1/\gamma$ differ only by a vertical shift because of the symmetry of the system.

The growth rate curve is now highly peaked, the asymptotic expressions for α and k_{max} being

$$\alpha = \frac{k^2}{3 + 2k^3\gamma}, \quad k_{max} = \left(\frac{3}{\gamma}\right)^{1/3}. \tag{3.4a, b}$$

Similar limiting behaviours occur for $r = 1$ (figure 2b), except that the finite depth of the upper layer strongly reduces the growth rate of the longest wavelengths. Figure 3 shows the most unstable wavenumber k_{max} as a function of r and γ. Canright & Morris (1993) discuss the various limiting forms of $\alpha(k)$.

I suppose that the initial perturbations have a single horizontal wavenumber k and one of three model planforms: rolls, squares, or hexagons. I denote the planform functions for these planforms by $R_i(q)$, $S_i(q)$, and $H_i(q)$, respectively, where i is a planform index and q is a dummy variable representing the horizontal wavenumber. The planforms at order ϵ have $i = 1$ and $q = k$; additional planforms with $i > 1$ and $q > k$ appear at order ϵ^2. The planforms for the $O(\epsilon)$ solutions are

$$R_1(q) = \cos qx, \tag{3.5a}$$

$$S_1(q) = \tfrac{1}{2}(\cos qx + \cos qy), \tag{3.5b}$$

$$H_1(q) = \frac{1}{3}\left[2\cos\frac{\sqrt{3}}{2}qx\cos\frac{q}{2}y + \cos qy\right]. \tag{3.5c}$$

In the roll and square planforms, maxima and minima have the same shape and amplitude. For hexagons, however, $H_1 = 1$ at the maxima (centres), and $-1/2$ at minima (corners). Accordingly, there is a difference between ‘up-hexagons’ with a positive amplitude $\epsilon > 0$, and ‘down-hexagons’ with $\epsilon < 0$.

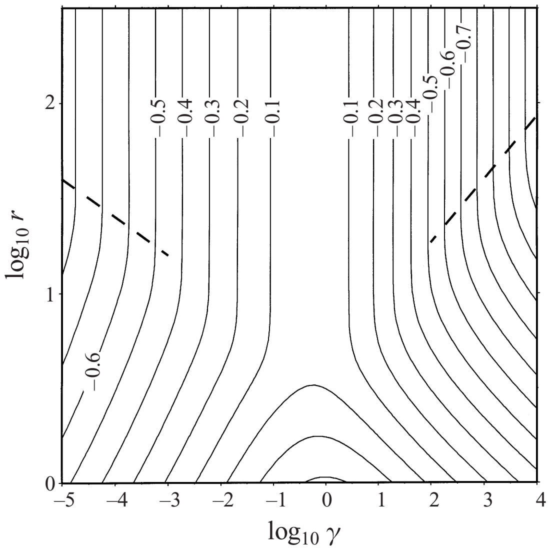

FIGURE 3. Most unstable wavenumber k_{max} as a function of viscosity contrast γ and depth ratio r. Annotations on the contours are values of $\log_{10} k_{max}$. Points above the dashed line on the left (slope $-1/5$) correspond to the 'hard-film' limit $k_{max} = (180\gamma)^{1/5}/2$, and points above the dashed line on the right (slope 1/3) to the 'soft-film' limit $k_{max} = (3/\gamma)^{1/3}$.

3.2. $O(\epsilon^2)$ *problem*

Proceeding now to order ϵ^2, one finds first that all the boundary and matching conditions satisfied by the toroidal potential Ψ_2 are homogeneous. This implies that $\Psi_2 = 0$, i.e. that the flow at order ϵ^2 is purely poloidal. A toroidal component of flow exists at order ϵ^3 for the square and hexagonal planforms if the layers have different viscosities ($\gamma \neq 1$), but determining it is beyond the scope of this study.

The poloidal scalar Φ_2 satisfies $\nabla^4 \Phi_2 = 0$, which must be solved subject to the matching conditions

$$\langle -\nabla_h^2 \Phi_2 \rangle = 0, \tag{3.6a}$$

$$\langle \nabla_h^2 \mathrm{D} \Phi_2 \rangle = -\frac{\Lambda_1}{k^2} \nabla_h \cdot (f \nabla_h f) \exp 2\alpha(k)t, \tag{3.6b}$$

$$\langle v \nabla_h^2 (\mathrm{D}^2 - \nabla_h^2) \Phi_2 \rangle = \frac{2\Lambda_2}{k^4} \left[2k^4 f^2 - 3k^2 |\nabla_h f|^2 + f_{xx}^2 + 2f_{xy}^2 + f_{yy}^2 \right] \exp 2\alpha(k)t, \tag{3.6c}$$

$$\langle -v \mathrm{D}(\mathrm{D}^2 + 3\nabla_h^2) \Phi_2 \rangle = -\eta_2, \tag{3.6d}$$

where

$$\Lambda_1 = k^2 \langle \mathrm{D}^2 \phi(0,k) \rangle, \quad \Lambda_2 = -k^4 \langle v \mathrm{D} \phi(0,k) \rangle, \tag{3.7a, b}$$

and v is the dimensionless viscosity ($= \gamma$ in the upper layer, 1.0 in the lower). Finally, the $O(\epsilon^2)$ part of the kinematic condition (2.6) is

$$\frac{\partial \eta_2}{\partial t} + \nabla_h^2 \Phi_2(0) = -\mathrm{D}\phi(0,k) \nabla_h \cdot (f \nabla_h f) \exp 2\alpha(k)t. \tag{3.8}$$

The inhomogeneous terms in (3.6*b*), (3.6*c*), and (3.8) correspond respectively to the three nonlinearities that drive the flow at order ϵ^2: effective discontinuities in the divergence of horizontal velocity and the divergence of the shear stress, and lateral self-advection of the interface. Only the last of these was considered by Daneš (1964) and Whitehead & Luther (1975).

The form of the matching conditions suggests that $\varPhi_2$ is a weighted sum of fundamental singular solutions with appropriate unit discontinuities at $z = 0$. Required for this study are three singular solutions $\phi(z, q)$, $\varphi(z, q)$, and $\chi(z, q)$, which represent the poloidal flows driven by discontinuities (with unit amplitude and horizontal wavenumber q) in the normal stress, the divergence of the shear stress, and the divergence of the horizontal velocity, respectively. The discontinuity in normal stress that drives $\phi(z, q)$ is defined to be negative for consistency with the previous definition of ϕ as the solution of the $O(\epsilon)$ problem. Explicit expressions for all three singular solutions are given in Appendix A.

The use of the singular solutions is best explained by example. Consider the case of rolls. Substitution of $f = R_1(k)$ into (3.6*b*) and (3.6*c*) yields

$$\left\langle \nabla_h^2 \mathrm{D} \varPhi_2 \right\rangle = \varLambda_1 R_1(2k) \exp 2\alpha(k)t, \tag{3.9}$$

$$\left\langle \nu \nabla_h^2 (\mathrm{D}^2 - \nabla_h^2) \varPhi_2 \right\rangle = 6\varLambda_2 R_1(2k) \exp 2\alpha(k)t. \tag{3.10}$$

Evidently $\varPhi_2$ is proportional to $R_1(2k)$, so that $\eta_2 = R_1(2k)g(t)$, where $g(t)$ is some function of time. The normal stress matching condition (3.6*d*) then becomes

$$\left\langle -\nu \mathrm{D}(\mathrm{D}^2 + 3\nabla_h^2) \varPhi_2 \right\rangle = -R_1(2k)g(t). \tag{3.11}$$

The solution for $\varPhi_2$ in each layer can now be expressed as a sum of three singular solutions with wavenumber $q = 2k$, each being weighted by the right-hand side of the corresponding matching condition:

$$\varPhi_2 = R_1(2k) \left\{ \phi(z, 2k)g(t) + [6\varLambda_2 \varphi(z, 2k) + \varLambda_1 \chi(z, 2k)] \exp 2\alpha(k)t \right\}. \tag{3.12}$$

The function $g(t)$ is determined by substituting (3.12) into (3.8) and solving the resulting differential equation subject to $g(0) = 0$. The solutions for squares and hexagons proceed similarly, except that the nonlinear interactions now generate additional horizontal modes with wavenumbers $\sqrt{2}k$ (squares) and $\sqrt{3}k$ (hexagons).

The results for all planforms can be expressed in terms of the quantity

$$\varPi(b) = \frac{k^2 [b^2 \varLambda_1 \chi(0, bk) + b^2(b^2 + 2)\varLambda_2 \varphi(0, bk) + \mathrm{D}\phi(0, k)]}{2\alpha(k) - \alpha(bk)}. \tag{3.13}$$

The three terms in the above expression correspond to the three nonlinearities identified earlier: effective jumps in the divergence of the horizontal velocity (first term) and the divergence of the shear stress (second term), and lateral advection of the interface (third term). However, the relative magnitudes of these three terms depend on the values of γ and r. In the hard-film limit, for example, the lower fluid sees the interface as traction-free, and the first term in (3.13) vanishes. In the soft-film limit, by contrast, the lower fluid sees the interface as a no-slip surface, and the second and third terms vanish. Asymptotic expressions for $\varPi(b)$ in the hard- and soft-film limits are given in Appendix B.

The solutions for η_2 can now be written down for the three model planforms. For rolls, the solution is

$$\eta_2 = \varPi(2)R_1(2k) [\exp 2\alpha(k)t - \exp \alpha(2k)t]. \tag{3.14}$$

For squares, the solution is

$$\eta_2 = \frac{\Pi(2)}{2} S_1(2k)\,[\exp 2\alpha(k)t - \exp \alpha(2k)t] + \frac{\Pi(\sqrt{2})}{2} S_2(\sqrt{2}k)[\exp 2\alpha(k)t - \exp \alpha(\sqrt{2}k)t], \tag{3.15}$$

where

$$S_2(\sqrt{2}k) = \cos kx \cos ky. \tag{3.16}$$

Finally, the solution for hexagons is

$$\begin{aligned} \eta_2 = {} & \frac{\Pi(2)}{3} H_1(2k)\,[\exp 2\alpha(k)t - \exp \alpha(2k)t] \\ & + \frac{\Pi(\sqrt{3})}{2} H_2(\sqrt{3}k)\left[\exp 2\alpha(k)t - \exp \alpha(\sqrt{3}k)t\right] \\ & + \frac{\Pi(1)}{6} H_1(k)\,[\exp 2\alpha(k)t - \exp \alpha(k)t]\,, \end{aligned} \tag{3.17}$$

where

$$H_2(\sqrt{3}k) = \frac{1}{3}\left[2\cos\frac{\sqrt{3}k}{2}x \cos\frac{3k}{2}y + \cos\sqrt{3}kx\right]. \tag{3.18}$$

The solutions above are valid for arbitrary values of k, γ, and r, and can be adapted to other boundary conditions at $z = -1$ and $z = r$ by modifying the singular solutions ϕ, φ, and χ accordingly.

4. Direction of spouting

If a perturbation of the interface is monochromatic and infinitesimal, its initial growth is purely exponential. After a finite time, however, the growth of maxima (or minima) becomes superexponential, and that of minima (or maxima), subexponential. Following Whitehead & Luther (1975), I shall call the onset of superexponential growth ‘spouting’, and the resulting structures ‘spouts’. Large-amplitude spouts are seen e.g. in the laboratory experiments of Whitehead & Luther (1975) and the numerical experiments of Newhouse & Pozrikidis (1990).

The direction of spouting (up or down) is controlled by the relative signs of η_1 and $\partial\eta_2/\partial t$ at interfacial extrema. If these quantities have the same sign, the growth rate of the extremum in question will be enhanced, and a spout will form; otherwise the extremum will flatten. The direction of spouting can therefore be determined by evaluating the quantity

$$\Gamma = \left[\frac{1}{\alpha(k)}\frac{\partial \eta_2}{\partial t}\right]_{t=0} \tag{4.1}$$

at interfacial maxima and minima (the factor $1/\alpha(k)$ serves merely to normalize the time derivative). Because the minima and maxima of the roll and square planforms R_1 and S_1 have the same form, it suffices to evaluate Γ at a maximum, say $(x, y) = (0, 0)$. Let the resulting values be Γ_R and Γ_S, respectively. For hexagons, Γ must be evaluated at two points: $(x, y) = (0, 0)$ (a centre of a hexagon defined by H_1) and $(x, y) = (2\sqrt{3}\pi/3k, 2\pi/3k)$ (a corner). Let the resulting values be Γ_H^+ and Γ_H^-, respectively.

Figure 4 shows Γ_R, Γ_S, Γ_H^+ and Γ_H^-, calculated assuming $k = k_{max}(\gamma, r)$, as functions of γ and r. Asymptotic expressions for these quantities in the hard- and soft-film limits

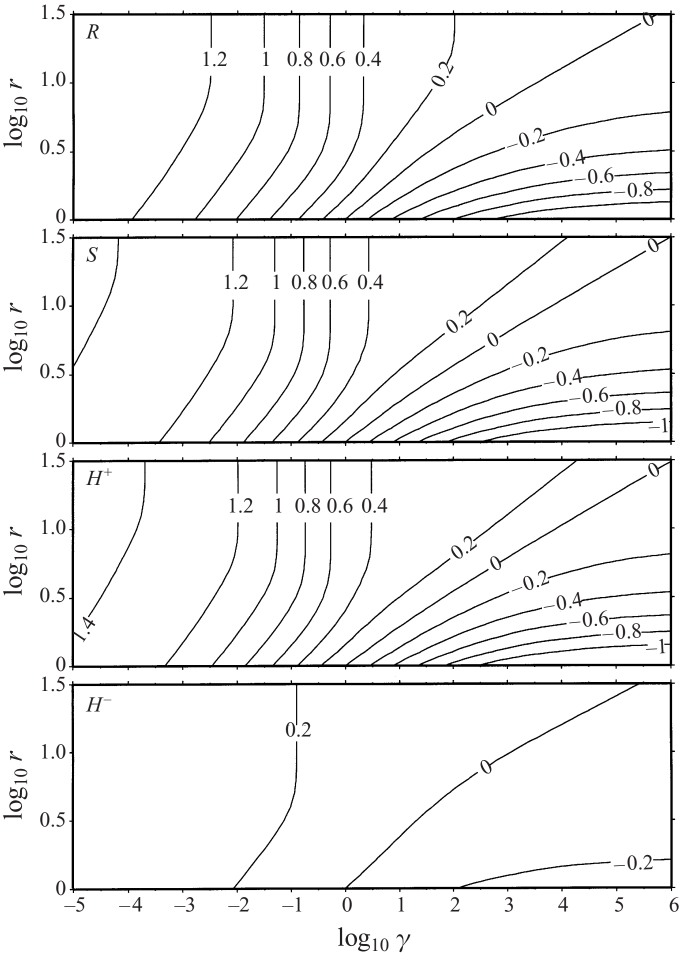

FIGURE 4. Normalized $O(\epsilon^2)$ growth rate Γ as a function of viscosity contrast γ and depth ratio r for (from top to bottom) rolls, squares, centres of hexagons, and corners of hexagons. Values of Γ are calculated assuming $k = k_{max}(\gamma, r)$ (see figure 3).

are given in Appendix B. For all planforms, $\Gamma > 0$ in the left and upper parts of the diagram, indicating that spouts of the lower fluid ascend from maxima. In the lower right portion of the diagram, however, $\Gamma < 0$, indicating that spouts of the upper fluid descend from minima. For rolls and squares, spouting at maxima (minima) is accompanied by flattening of the minima (maxima). For hexagons, the origin of the spouts depends on the sign of ϵ. If $\epsilon > 0$ (up-hexagons), spouts ascend from the centres when $\Gamma_H^+ > 0$ and descend from the corners when $\Gamma_H^- < 0$. If however $\epsilon < 0$, spouts descend from the centres when $\Gamma_H^+ < 0$ and ascend from the corners when $\Gamma_H^- > 0$.

Figure 4 shows that there exists a critical value of the thickness ratio $r = r_c(\gamma)$ at which the spouting direction changes. The physical reason for this is simple. The lower and upper extremities of figure 4 show that (i) if the layers have equal thickness ($r = 1$), the spouts penetrate the less viscous layer, and (ii) if one of the layers (i.e. the upper) is infinitely thick, the spouts penetrate this layer regardless of the viscosity contrast. Spouts thus tend to penetrate the layer that is less viscous and thicker.

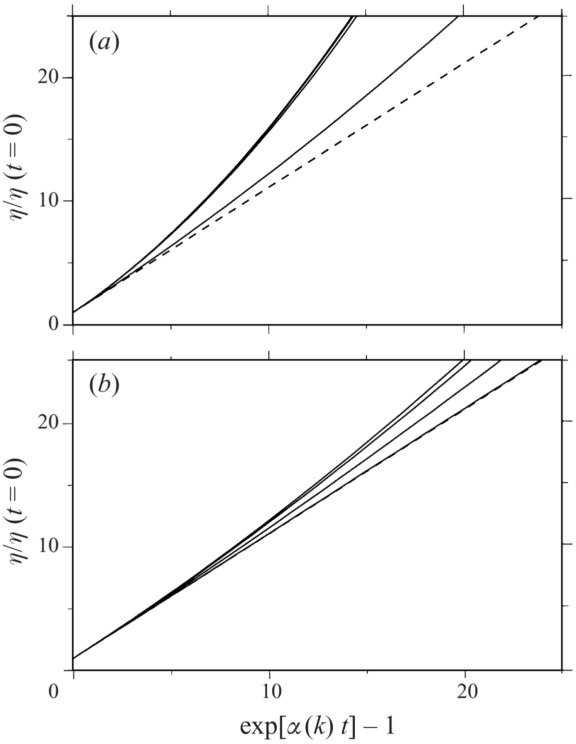

FIGURE 5. Normalized spout amplitude as a function of time in the (*a*) hard- and (*b*) soft-film limits, for $|\epsilon| = 0.03$. Dashed line represents the exponential growth of an infinitesimal ($|\epsilon| \to 0$) perturbation. The four solid lines in each diagram are for (from top to bottom) hexagons with central spouts, squares, rolls, and hexagons with corner spouts. In the hard-film limit, the two uppermost curves (hexagons with central spouts and squares) are indistinguishable. In the soft-film limit, the lowermost curve (hexagons with corner spouts) is barely distinguishable from purely exponential growth.

When $\gamma > 1$, however, the more viscous layer is thicker, and the two tendencies are opposed. Consequently there must exist a critical value of $r = r_c$ at which they balance each other, and at which the spouting direction changes. The critical curves shown in figure 4 substantiate and quantify the suggestion of Daneš (1964), Whitehead & Luther (1975), and Fermigier *et al.* (1992) that the spouting direction is determined by the relative 'resistances' of the layers.

The sensitivity of the spouting direction to changes in the relative thicknesses and viscosities of the layers is measured by the slope $m \equiv \mathrm{d}\ln r/\mathrm{d}\ln\gamma$ of the critical curve $r = r_c(\gamma)$. For hexagons with central spouts (H^+), for example, $0.230 \leqslant m \leqslant 0.286$. The results for the other planforms are similar. The smallness of the slope means that the spouting direction is much more sensitive to the thicknesses of the layers than to their viscosities.

Understanding the evolution of the instability for points (γ, r) on the critical curve would require carrying the solution to order ϵ^3, and is beyond the scope of this study. However, one may anticipate that the maxima and minima of the perturbed interface will initially evolve as mirror images of each other, with the same shape and growth rate. This expectation is confirmed by finite-amplitude numerical solutions for rolls (H. Schmeling, personal communication, 1998). However, no spouting occurs in these solutions: the growth rates are everywhere subexponential after finite time.

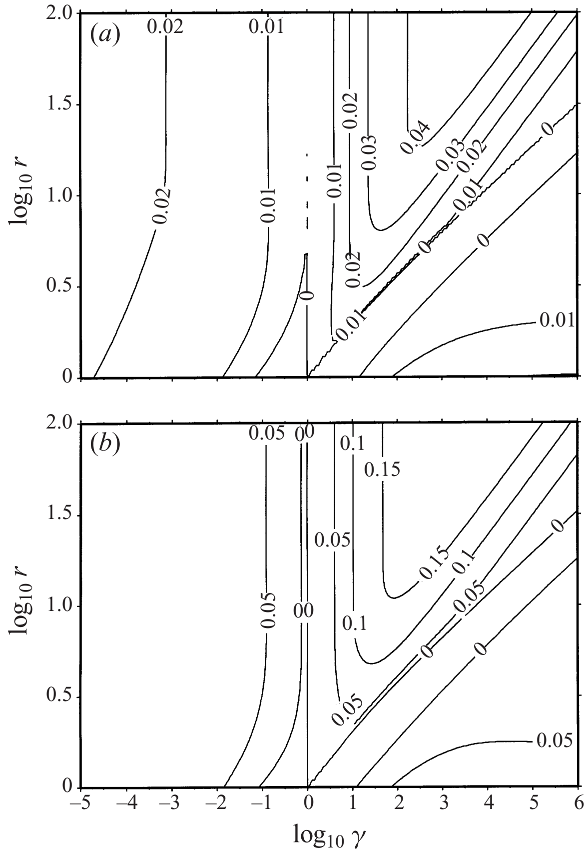

FIGURE 6. Planform selectivity indices (*a*) $\Sigma_{HS} = |\Gamma_H^+| - |\Gamma_S|$ and (*b*) $\Sigma_{HR} = |\Gamma_H^+| - |\Gamma_R|$ as functions of γ and r.

5. Planform selection

The solution obtained above predicts the relative growth rates of the model planforms as functions of γ and r. The end-member behaviours are illustrated by the hard- and soft-film limits. Figure 5 shows the amplitude of the spouts in these limits as a function of time, for $|\epsilon| = 0.03$ and $k = k_{max}(\gamma, r)$. The dashed lines represent the purely exponential growth that obtains for $|\epsilon| \rightarrow 0$. In the hard-film limit (*a*), the growth rate of all planforms quickly becomes superexponential. However, the growth rates for rolls, squares, and up-hexagons (spouts ascending from centres), are nearly indistinguishable from one another. Moreover, the growth of down-hexagons (spouts ascending from corners) is much slower than that of the other planforms. In the soft-film limit (*b*), by contrast, the growth remains exponential longer than in the hard-film limit, but the eventual departures from this differ significantly among planforms. The curve for down-hexagons is nearly indistinguishable from purely exponential growth.

The order of planform preference shown in figure 5 for $r = \infty$ generally obtains for finite r also. Figure 6 shows 'planform selectivity indices' $\Sigma_{HS} = |\Gamma_H^+| - |\Gamma_S|$ and $\Sigma_{HR} = |\Gamma_H^+| - |\Gamma_R|$ as functions of γ and r. These indices measure the nonlinear amplification of hexagons with central spouts relative to that of squares and rolls, respectively. The analogous index for hexagons with corner spouts was not calculated because the growth of this planform is too slow to be of interest. Figure 5 shows that

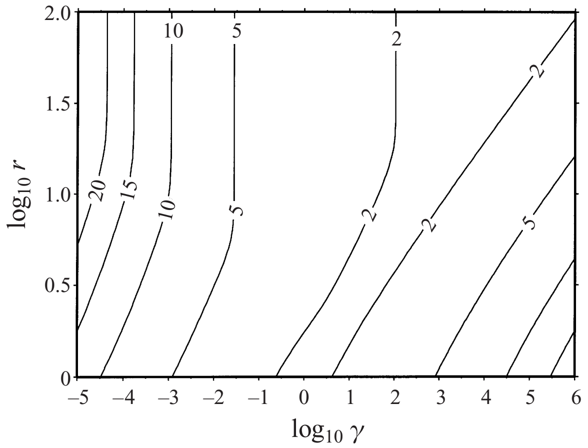

FIGURE 7. Half-bandwidth $B = (k_+ - k_{max})/k_{max}$ as a function of γ and r. Wavenumber $k_+ > k_{max}$ is that whose growth rate is one half the maximum value $\alpha(k_{max})$.

hexagons with central spouts are (slightly) preferred to squares, and both of these planforms preferred to rolls, for nearly all values of γ and r, except just to the left of the line $\gamma = 1$. The slightly negative values of Σ_{HR} and Σ_{HS} between the zero contours for $\gamma > 1$ are not meaningful because the neglected $O(\epsilon^3)$ solution becomes important when $r \approx r_c$.

Figure 5 suggests that there is an inverse relationship between nonlinear amplification of the growth rate and planform selectivity. This can be explained to first order by the shape of the peak of the growth rate curve $\alpha(k)$ predicted by the linear theory (Biot 1961; Johnson & Fletcher 1994). When the peak is broad and flat, the harmonics generated by the nonlinear interactions have nearly the same (linear) growth rate as the fundamental mode, so amplification is high. But because the growth rates of all harmonics are nearly equal, no planform is strongly preferred. When the peak of the growth rate curve is sharp, by contrast, the opposite situation obtains: nonlinear amplification is low, but planform selectivity is high. Biot (1961) measured the selectivity in terms of the 'relative bandwidth' $(k_+ - k_-)/k_{max}$, where $k_+ > k_{max}$ and $k_- < k_{max}$ are the wavenumbers whose growth rates are one half the maximum value $\alpha(k_{max})$. Because only wavenumbers $k \geqslant k_{max}$ appear in the problem studied here, I use instead the half-bandwidth

$$B = \frac{(k_+ - k_{max})}{k_{max}}, \tag{5.1}$$

which is shown as a function of γ and r in figure 7. Comparison of figure 7 with figure 6 shows that smaller bandwidths generally correspond to higher selectivity, as expected. The planform selectivity is relatively strong when $\gamma \geqslant 10$ and $r \geqslant \gamma^{1/3}$, and reaches its maximum ($\Sigma_{HS} = 0.181$, $\Sigma_{HR} = 0.043$) in the soft-film limit, where $B = 1.94$.

The planform 'pecking order' found above (hexagons with central spouts, squares, rolls, hexagons with corner spouts) is identical to that found by Fermigier *et al.* (1992) for the RT instability of a thin viscous film exposed to air. The behaviour of that system is dominated by surface tension, which limits the instability to long wavelengths. Such a system has a half-bandwidth $B = 0.307$, and is therefore more selective than the one studied here.

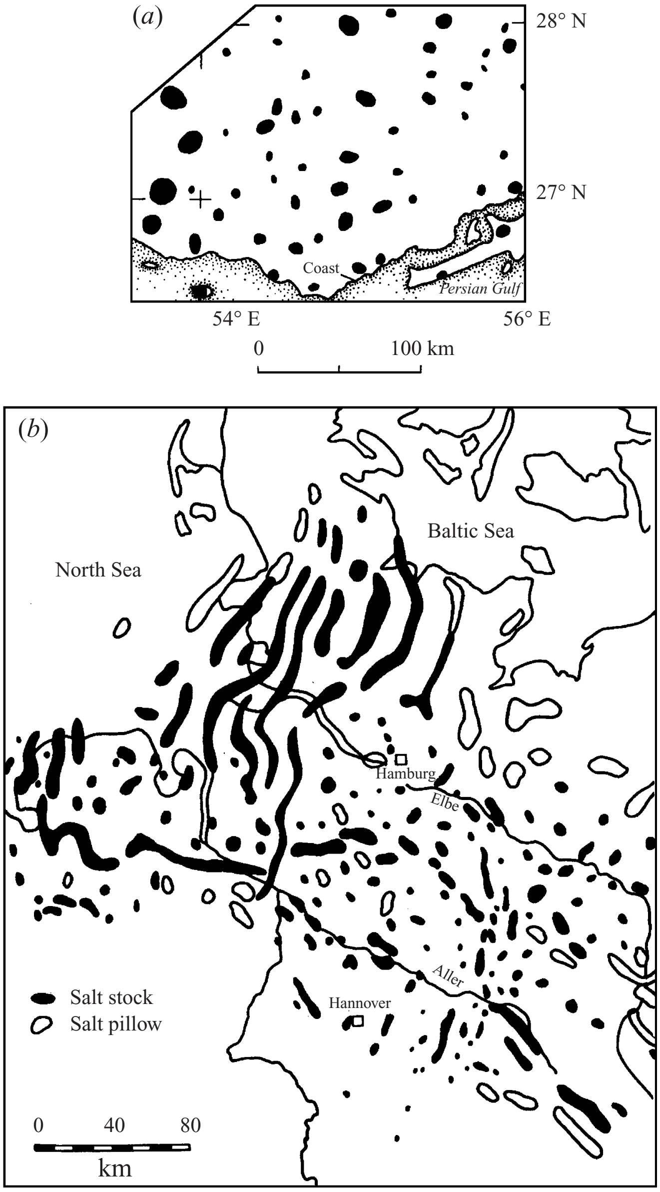

FIGURE 8. Distribution of salt domes in (*a*) the Zagros Mountains of Iran (from Jackson *et al.* 1990) and (*b*) the Zechstein Basin of Germany (from Trusheim 1960, reprinted by permission of the American Association of Petroleum Geologists).

6. Application to salt tectonics

Salt domes are buoyant structures that form when salt deposited in a sedimentary basin or shallow sea rises through a subsequently deposited layer of sediment. Salt domes typically occur in families of several tens or hundreds; well-known examples are found in the Gulf Coast of the United States, the Zechstein basin in northern Germany, and the Great Kavir desert in central Iran. A global survey of salt dome fields can be found in Jackson, Roberts & Snelson (1995).

Understanding the formation of salt domes is important for several reasons. First, a

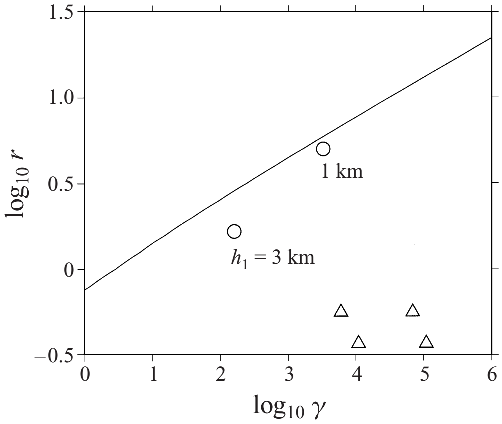

FIGURE 9. Critical curve $r = r_c$ for hexagons with central spouts (solid line), together with values (γ, r) consistent with the observed spacing L of salt domes in the Zagros Mountains (circles) and the Zechstein basin (triangle). Points for the Zagros Mountains correspond to the estimates of h_1 shown. Scatter of the points for the Zechstein basin reflects uncertainties of h_1, h_2, and L. Critical curve shown is for a rigid surface beneath the salt layer.

large fraction of the world's hydrocarbon reserves is associated with such structures, which readily trap rising oil and gas due to their low permeability. For the same reason, salt domes are prime candidates for storage of radioactive waste; choosing suitable domes for this purpose requires a detailed understanding of their structure (Jackson & Talbot 1989). More fundamentally, salt domes are a striking example of large-scale natural pattern formation. Figure 8 shows the geographical distribution of salt domes in the Zechstein basin and in the Zagros Mountains of southern Iran. Particularly noteworthy is the transition in the Zechstein basin from a roughly two-dimensional pattern ('salt walls') in the northwest to a three-dimensional pattern in the southeast.

The classic model for salt domes is that of a RT instability that occurs when the sediments become denser than the underlying salt due to progressive compaction (Nettleton 1934; Daneš 1964; Selig 1965). This model is of course applicable only if the sediments can reasonably be assumed to behave fluidly (Weijermars, Jackson & Vendeville 1993); this is most likely when they contain substantial quantities of distributed evaporites, as in the Great Kavir and Zagros Mountain regions of Iran (Jackson *et al.* 1990). The traditional application of the model is to use the linear theory to determine the sediment/salt viscosity contrast for which the observed dome spacing L corresponds to the fastest growing wavelength, given estimates of the initial layer thicknesses h_1 and $h_2 = rh_1$ (Rönnlund 1989; Jackson *et al.* 1990). It is of interest to determine where the resulting points (γ, r) lie relative to the critical curve $r = r_c(\gamma)$ that controls the direction of spouting. Consider first the case of the Zagros Mountains, where $L = 28$ km, $h_2 = 5$ km, and 1 km $\leqslant h_1 \leqslant$ 3 km (Jackson *et al.* 1990). Figure 9 shows the values (γ, r) predicted by the linear theory for h_1 =1 km and 3 km (circles), together with the critical curve $r = r_c(\gamma)$ for hexagons. The points (γ, r) and the critical curve were calculated after replacing the free-slip boundary condition at the bottom of the salt layer by a more geologically realistic rigid surface condition. Because the top and bottom boundary conditions are now different, the critical curve no longer passes through $(\gamma, r) \equiv (1, 1)$. The predicted points (γ, r) lie below the critical curve, indicating that the direction of spouting is downward, i.e. into the salt layer. A similar result is found for the Zechstein basin. Rönnlund (1989) applied the linearized RT model to a portion of the basin west of Bremen, where 900 m $\leqslant h_1 \leqslant$ 1100 m, 400 m $\leqslant h_2 \leqslant$ 500 m, and 8 km $\leqslant L \leqslant$ 12 km (Jaritz 1973). The predicted values of (γ, r) that correspond to these estimates (triangles in figure 9) are again below the critical curve, indicating that spouting is downward. Physically, this means that the portion of the salt layer beneath the spout drains rapidly (i.e. superexponentially) into the rest of the layer, which itself thickens subexponentially and eventually forms a salt dome. This behaviour is confirmed by finite-amplitude numerical solutions (H. Schmeling, personal communication, 1998).

The nonlinear theory presented here also provides some insight into the origin of the planforms of figure 8. Figure 6 shows that when (γ, r) lies below the critical curve, hexagons and squares have nearly the same growth rate and both grow substantially faster than rolls. The same result obtains with only slight qualitative differences when the bottom boundary is rigid, as assumed in this section. One would therefore expect the preferred planform to be an irregular polygonal pattern, as observed for most of the Zechstein and Zagros regions. This expectation is confirmed by laboratory experiments, in which the planform is dominated by an irregular 'spoke' pattern and rolls are confined to within two wavelengths of sidewalls (Talbot *et al.* 1991). However, the roll-like 'salt walls' in the Zechstein basin probably reflect the influence of crustal faults, which are observed to trend in the same direction (Nalpas & Brun 1993). This implies that the distribution of the salt in this part of the basin may be controlled by large-scale extension of a brittle (rather than fluid) crust. Applications of the RT model to the Zechstein basin should therefore be interpreted with caution.

7. Summary and conclusions

(i) I have examined the weakly nonlinear evolution of the Rayleigh–Taylor (RT) instability of two superposed layers of viscous fluid between impermeable and traction-free planes in a field of gravity. I obtain analytical solutions valid to second order in the small amplitude of the initial perturbation of the interface, which consists of either rolls or squares or hexagons with a horizontal wavenumber k. The solutions are valid for arbitrary values of k, the viscosity ratio (upper/lower) γ, and the depth ratio r. For simplicity, however, I assume $k = k_{max}(\gamma, r)$, where k_{max} is the most unstable wavenumber.

(ii) The flow is purely poloidal to order ϵ^2. However, a toroidal component with non-zero vertical vorticity enters at order ϵ^3 for the square and hexagonal planforms if the fluids have different viscosities ($\gamma \neq 1$).

(iii) The flow at order ϵ^2 is driven by three distinct nonlinearities: effective jumps at $z = 0$ in (*a*) the divergence of the horizontal velocity and (*b*) the divergence of the shear stress, and (*c*) lateral self-advection of the interface. The relative importance of these three mechanisms varies as a function of γ and r. In the 'hard-film' limit of a thin high-viscosity layer beneath a deep low-viscosity fluid, only mechanisms (*b*) and (*c*) operate. In the 'soft-film' limit of a thin low-viscosity layer beneath a deep high-viscosity fluid, only mechanism (*a*) operates.

(iv) For all planforms, the direction of spouting (superexponential growth of interfacial extrema) is determined by the balance between tendencies to penetrate the less viscous and the thicker layer. When these tendencies are opposed (i.e. when $\gamma > 1$ for $r > 1$), the spouts change direction at a critical value of $r = r_c(\gamma)$. The small slope ($\mathrm{d}\ln r/\mathrm{d}\ln \gamma < 0.36$) of the critical curve implies that the direction of spouting is much more sensitive to the thicknesses of the layers than to their viscosities.

(v) For nearly all values of γ and r, the most rapidly growing planforms are (in descending order) hexagons with central spouts, squares, rolls, and hexagons with corner spouts. However, squares grow almost as fast as hexagons with central spouts, and hexagons with corner spouts grow much more slowly than the other three planforms.

(vi) The instability exhibits an inverse relationship between nonlinear growth rate amplification and planform selectivity. The selectivity is inversely proportional to the bandwidth of the growth rate curve for infinitesimal perturbations, and is highest when $\gamma > 10$ and $r \geqslant \gamma^{1/3}$.

(vii) A classic geological application of the RT model is to the formation of salt domes in the Earth's crust. The traditional procedure is to use the linear theory to determine the sediment/salt viscosity contrast for which the observed dome spacing corresponds to the fastest growing wavelength, given estimates of the initial layer thicknesses. For salt domes in Germany and Iran, the resulting estimates (γ, r) lie below the critical curve $r = r_c(\gamma)$, indicating that the domes developed from interfacial extrema that grew subexponentially. The dominantly polygonal planform of these domes is consistent with the model prediction that hexagons and squares have nearly the same growth rate and that both grow faster than rolls.

This research was supported by NSF grant 97-07604 and by funds from the Institut de Physique du Globe (Paris). I am grateful to C. J. Allègre, V. Courtillot, and C. Jaupart for inviting me to visit IPG, and to C. Jaupart for offering me the hospitality of his laboratory. M. Brandon, R. Fletcher, and M. P. A. Jackson guided me through the literature on salt domes. I thank A. Davaille for helpful discussions, G. Houseman and H. Schmeling for careful reviews, and H. Schmeling for carrying out finite-amplitude numerical solutions. Algebraic manipulations were performed using Mathematica (Wolfram 1996). Figures were prepared using the GMT software package (Wessel & Smith 1995). The American Association of Petroleum Geologists kindly granted permission to reproduce figure 8(*b*).

Appendix A. Singular solutions

This Appendix gives explicit expressions for the three singular solutions $\phi(z,q)$, $\varphi(z,q)$, and $\chi(z,q)$. Each (generic name $G(z,q)$) satisfies the equation $(\mathrm{D}^2 - q^2)^2 G = 0$ and the boundary conditions $G(r,q) = G(-1,q) = \mathrm{D}^2 G(r,q) = \mathrm{D}^2 G(-1,q) = 0$. The matching conditions they satisfy are

$$\langle \phi \rangle = \langle -q^2 \mathrm{D}\phi \rangle = \langle -\nu q^2 (\mathrm{D}^2 + q^2)\phi \rangle = \langle -\nu \mathrm{D}(\mathrm{D}^2 - 3q^2)\phi \rangle + 1 = 0, \qquad (\mathrm{A}\,1a)$$

$$\langle \varphi \rangle = \langle -q^2 \mathrm{D}\varphi \rangle = \langle -\nu q^2 (\mathrm{D}^2 + q^2)\varphi \rangle - 1 = \langle -\nu \mathrm{D}(\mathrm{D}^2 - 3q^2)\varphi \rangle = 0, \qquad (\mathrm{A}\,1b)$$

$$\langle \chi \rangle = \langle -q^2 \mathrm{D}\chi \rangle - 1 = \langle -\nu q^2 (\mathrm{D}^2 + q^2)\chi \rangle = \langle -\nu \mathrm{D}(\mathrm{D}^2 - 3q^2)\chi \rangle = 0. \qquad (\mathrm{A}\,1c)$$

In the following formulae, q is a dummy variable representing the horizontal wavenumber, $p = 2q$, $P = 2qr$, $s = \sinh p$, $S = \sinh P$, $c = \cosh p$, $C = \cosh P$, n (= 1 or 2) is the layer index, $d_1 = -1$, and $d_2 = r$:

$$\varDelta = (S - P)(s + p) + 2\gamma(Cc - 1 + Pp) + \gamma^2 (S + P)(s - p), \qquad (\mathrm{A}\,2)$$

$$\alpha = \frac{(S - P)(c - 1) + \gamma(s - p)(C - 1)}{p\varDelta}, \qquad (\mathrm{A}\,3)$$

$$\phi_n = A_n \sinh q(z - d_n) + B_n q(z - d_n) \cosh q(z - d_n), \qquad (\mathrm{A}\,4)$$

$$A_1 = \frac{1}{2q^3\Delta}\{[2(S-P)+\gamma p(C-1)]\sinh q \\ +[p(S-P)+\gamma(pP+2(C-1))]\cosh q\} \qquad \text{(A 5}a\text{)}$$

$$A_2 = \frac{-1}{2q^3\Delta}\{[2\gamma(s-p)+P(c-1)]\sinh qr, \\ +[\gamma P(s-p)+Pp+2(c-1)]\cosh qr\}, \qquad \text{(A 5}b\text{)}$$

$$B_1 = \frac{-1}{q^3\Delta}\{(S-P+\gamma P)\sinh q+\gamma(C-1)\cosh q\}, \qquad \text{(A 5}c\text{)}$$

$$B_2 = \frac{1}{q^3\Delta}\{[\gamma(s-p)+p]\sinh qr+(c-1)\cosh qr\}, \qquad \text{(A 5}d\text{)}$$

$$\varphi_n = C_n\sinh q(z-d_n)+D_nq(z-d_n)\cosh q(z-d_n), \qquad \text{(A 6)}$$

$$C_1 = \frac{-1}{q^3\Delta}\{[S+P(\gamma-1)]\sinh q+\gamma(C+1+2r)\cosh q\}, \qquad \text{(A 7}a\text{)}$$

$$C_2 = \frac{-1}{q^3\Delta}\{r[\gamma(s-p)+p]\sinh qr+[r(c+1)+2]\cosh qr\}, \qquad \text{(A 7}b\text{)}$$

$$D_1 = \frac{1}{q^4\Delta}\{\gamma(C+1)\sinh q+[S+P(\gamma-1)]\cosh q\}, \qquad \text{(A 7}c\text{)}$$

$$D_2 = \frac{1}{q^4\Delta}\{(c+1)\sinh qr+[\gamma(s-p)+p]\cosh qr\}, \qquad \text{(A 7}d\text{)}$$

$$\chi_n = J_n\sinh q(z-d_n)+K_nq(z-d_n)\cosh q(z-d_n), \qquad \text{(A 8)}$$

$$J_1 = \frac{-2\gamma}{q^2\Delta}\{(C-1-2r)\sinh q+[\gamma(S+P)-P]\cosh q\}, \qquad \text{(A 9}a\text{)}$$

$$J_2 = \frac{2}{q^2\Delta}\{\gamma[r(c-1)-2]\sinh qr+r[s+p(1-\gamma)]\cosh qr\}, \qquad \text{(A 9}b\text{)}$$

$$K_1 = \frac{2\gamma}{q^3\Delta}\{[\gamma(S+P)-P]\sinh q+(C-1)\cosh q\}, \qquad \text{(A 9}c\text{)}$$

$$K_2 = \frac{-2}{q^3\Delta}\{[s+p(1-\gamma)]\sinh qr+\gamma(c-1)\cosh qr\}. \qquad \text{(A 9}d\text{)}$$

Appendix B. Asymptotic expressions

All the expressions below are calculated assuming $k = k_{max}$, where k_{max} is given by (3.3*b*) (hard-film limit) or (3.4*b*) (soft-film limit). In the hard-film limit,

$$\Pi(b) \sim \frac{5}{4}+\frac{1}{2b^2}, \qquad \text{(B 1)}$$

$$\Gamma_R \sim \frac{11}{8} \approx 1.38, \quad \Gamma_S \sim \frac{23}{16} \approx 1.44, \qquad \text{(B 2}a,b\text{)}$$

$$\Gamma_H^+ \sim \frac{35}{24} \approx 1.46, \quad \Gamma_H^- \sim \frac{1}{3} \approx 0.33. \qquad \text{(B 2}c,d\text{)}$$

In the soft-film limit,

$$\Pi(b) \sim \frac{3}{4b^3 - 3b^2 + 2}, \tag{B 3}$$

$$\Gamma_R \sim \frac{3}{17} \approx 0.176, \quad \Gamma_S \sim \frac{21 + 102\sqrt{2}}{527} \approx 0.314, \tag{B 4a,b}$$

$$\Gamma_H^+ \sim \frac{1154 + 459\sqrt{3}}{5457} \approx 0.357, \quad \Gamma_H^- \sim \frac{-2767 + 1836\sqrt{3}}{21828} \approx 0.019. \tag{B 4c,d}$$

REFERENCES

Babchin, A. J., Frenkel, A. L., Levich, B. G. & Sivashinsky, G. I. 1983 Nonlinear saturation of Rayleigh–Taylor instability in thin films. *Phys. Fluids* **26**, 3159–3161.

Biot, M. A. 1961 Theory of folding of stratified viscoelastic media and its implications in tectonics and orogenesis. *Geol. Soc. Am. Bull.* **72**, 1595–1620.

Canright, D. & Morris, S. 1993 Buoyant instability of a viscous film over a passive fluid. *J. Fluid Mech.* **255**, 349–372.

Chandrasekhar, S. 1961 *Hydrodynamic and Hydromagnetic Stability*. Oxford University Press.

Daneš, Z. F. 1964 Mathematical formulation of salt dome dynamics. *Geophys.* **29**, 414–424.

Fermigier, M., Limat, L., Wesfreid, J. E., Boudinet, P. & Quilliet, C. 1992 Two-dimensional patterns in Rayleigh–Taylor instability of a thin layer. *J. Fluid Mech.* **236**, 349–383.

Fletcher, R. C. 1972 Application of a mathematical model to the emplacement of mantled gneiss domes. *Am. J. Sci.* **272**, 197–216.

Houseman, G. A. & Molnar, P. 1997 Gravitational (Rayleigh–Taylor) instability of a layer with non-linear viscosity and convective thinning of continental lithospere. *Geophys. J. Intl* **128**, 125–150.

Jackson, M. P. A., Craig, C. H., Gansser, A., Stocklin, J. & Talbot, C. J. 1990 Salt diapirs of the Great Kavir, Central Iran. *Geol. Soc. Am. Memoir* 177.

Jackson, M. P. A., Roberts, D. G. & Snelson, S. (eds.) 1995 Salt tectonics: a global perspective. *Am. Assoc. Petrol. Geol. Memoir* 65.

Jackson, M. P. A. & Talbot, C. J. 1989 Anatomy of mushroom-shaped diapirs. *J. Struct. Geol.* **11**, 211–230.

Jacobs, J. W. & Catton, I. 1988 Three-dimensional Rayleigh–Taylor instability. Part 1. Weakly nonlinear theory. *J. Fluid Mech.* **187**, 329–352.

Jaritz, W. 1973 Zur Entstehung der Salzstrukturen Nordwestdeutschlands. *Geol. Jahrb.* A **10**, 3–77.

Johnson, A. M. & Fletcher, R. C. 1994 *Folding of Viscous Layers*. Columbia University Press.

Marsh, B. D. & Carmichael, I. S. E. 1974 Benioff zone magmatism. *J. Geophys. Res.* **79**, 1196–1206.

Nalpas, T. & Brun, J.-P. 1993 Salt flow and diapirism related to extension at crustal scale. *Tectonophys.* **228**, 349–362.

Nettleton, L. L. 1934 Fluid mechanics of salt domes. *Bull. Am. Assoc. Petrol. Geol.* **18**, 1175–1204.

Newhouse, L. A. & Pozrikidis, C. 1990 The Rayleigh–Taylor instability of a viscous liquid layer resting on a plane wall. *J. Fluid Mech.* **217**, 615–638.

Ramberg, H. 1981 *Gravity, Deformation, and the Earth's Crust in Theory, Experiments, and Geological Application*, 2nd. edn. Academic.

Rayleigh, Lord 1883 Investigation of the character of an incompressible heavy fluid of variable density. *Proc. Lond. Math. Soc.* **14**, 170–197.

Rönnlund, P. 1989 Viscosity ratio estimates from natural Rayleigh–Taylor instabilities. *Terra Nova* **1**, 344–348.

Schmeling, H. 1987 On the relation between initial conditions and late stages of Rayleigh–Taylor instabilities. *Tectonophys.* **133**, 65–80.

Selig, F. 1965 A theoretical prediction of salt dome patterns *Geophys.* **30**, 633–643.

Talbot, C. J., Rönnlund, P., Schmeling, H., Koyi, H. & Jackson, M. P. A. 1991 Diapiric spoke patterns. *Tectonophys.* **188**, 187–201.

Taylor, G. I. 1950 The instability of liquid surfaces when accelerated in a direction perpendicular to their planes. I. *Proc. R. Soc. Lond.* A **201**, 192–196.

Trusheim, F. 1960 Mechanism of salt migration in northern Germany. *Bull. Am. Assoc. Petrol. Geol.* **44**, 1519–40.

Weijermars, R., Jackson, M. P. A. & Vendeville, B. 1993 Rheological and tectonic modeling of salt provinces. *Tectonophys.* **217**, 143–174.

Wessel, P. & Smith, W. H. F. 1995 New version of the Generic Mapping Tools released. *EOS Trans. Am. Geophys. Un.* **76**, 329.

Whitehead, J. A. 1986 Buoyancy-driven instabilities of low-viscosity zones as models of magma-rich zones. *J. Geophys. Res.* **91**, 9303–9314.

Whitehead, J. A. & Luther, D. S. 1975 Dynamics of laboratory diapir and plume models. *J. Geophys. Res.* **80**, 705–717.

Woidt, W.-D. 1978 Finite element calculations applied to salt dome analysis. *Tectonophys.* **50**, 369–386.

Wolfram, S. 1996 *The Mathematica Book*, 3rd edn. Wolfram Media/Cambridge University Press.

Yiantsios, S. G. & Higgins, B. G. 1989 Rayleigh–Taylor instability in thin viscous films. *Phys. Fluids* **31**, 440–446.